Biophysical*Journal*
Article

Biophysical Society

Structure of Galectin-3 bound to a model membrane containing ganglioside GM1

Crystal M. Vander Zanden,[1,*] Jaroslaw Majewski,[2,3,4] Yvonne Weissbarth,[1] Danielle F. Browne,[1] Erik B. Watkins,[5] and Hans-Joachim Gabius[6]

[1]Department of Chemistry and Biochemistry, University of Colorado at Colorado Springs, Colorado Springs, Colorado; [2]Division of Molecular and Cellular Biology, National Science Foundation, Alexandria, Virginia; [3]Department of Chemical and Biological Engineering and Center for Biomedical Engineering, University of New Mexico, Albuquerque, New Mexico; [4]Theoretical Biology & Biophysics, Los Alamos National Laboratory, Los Alamos, New Mexico; [5]MPA-11: Materials Synthesis and Integrated Devices, Los Alamos National Laboratory, Los Alamos, New Mexico; and [6]Institute of Physiological Chemistry, Faculty of Veterinary Medicine, Ludwig-Maximilians-University Munich, Planegg, Germany

ABSTRACT Galectin-3 (Gal-3) is a β-galactosidase-binding protein involved in various biological processes, including neuronal growth and adhesion. The pairing of Gal-3 with ganglioside GM1's pentasaccharide chain at the outer leaflet of the plasma membrane, which triggers downstream cell-signaling cascades, seems to be involved in these processes. A crucial feature of Gal-3 is its ability to form oligomers and supramolecular assemblies that connect various carbohydrate-decorated molecules. Although we know the atomistic structure of Gal-3 bound to small carbohydrate ligands, it remains unclear how Gal-3 binds GM1 in a membrane. Furthermore, the influence of this interaction on Gal-3's structure and oligomeric assembly has to be elucidated. In this study, we used X-ray reflectivity (XR) from a model membrane to determine the structure and surface coverage of Gal-3 bound to a membrane containing GM1. We observed that the carbohydrate recognition domain interacts with GM1's pentasaccharide, while the N-terminal domain is pointed away from the membrane, likely to facilitate protein-protein interactions. In a membrane containing 20 mol % GM1, Gal-3 covered ∼50% of the membrane surface with one Gal-3 molecule bound per 2130 Å^2. We used molecular dynamics simulations and Voronoi tessellation algorithms to build an atomistic model of membrane-bound Gal-3, which is supported by the XR results. Overall, this work provides structural information describing how Gal-3 can bind GM1's pentasaccharide chain, a prerequisite for triggering regulatory processes in neuronal growth and adhesion.

SIGNIFICANCE Galectin-3 (Gal-3) is a carbohydrate-binding protein that regulates cell growth and adhesion in neurons. Gal-3 does this through interactions with ganglioside GM1, a carbohydrate-decorated lipid on the cell membrane's outer surface. This work proposes a structure for galectin-3 bound to GM1 to better understand how galectin-3 regulates neuronal function.

INTRODUCTION

Galectins are a family of proteins that bind to β-galactosidase-containing carbohydrates via a 130–140 residue carbohydrate recognition domain (CRD) (1,2). The CRD is composed of five- and six-stranded antiparallel β sheets arranged in a "jelly roll" fold that is highly conserved among all galectins, despite the proteins only sharing ∼30% sequence identity (3). In the CRD, affinity for carbohydrates is driven by a combination of polar contacts and CH-π interactions with aromatic sidechains belonging to a typical signature sequence (4–7). There are three types of design of vertebrate galectins (8). The first has CRDs arranged as a non-covalent homodimer (proto-type), e.g., galectin-1, which exists in a reversible monomer/dimer equilibrium. In this proto-type galectin structure, each CRD cooperatively influences the other's affinity for ligand binding (9–11). The second type has CRDs connected by a polypeptide linker in a heterodimeric tandem-repeat-type display. In this modular arrangement, linker length and flexibility influence galectin supramolecular assembly (12). The third arrangement, chimera-type, is only found in wild-type galectin-3 (WT Gal-3; Fig. 1). The trimodular protein consists of a ∼120 amino acid N-terminal domain containing

---

Submitted July 6, 2022, and accepted for publication August 15, 2022.

*Correspondence: cvanderz@uccs.edu

Hans-Joachim Gabius passed away on August 2nd 2021, prior to submission of the manuscript.

Editor: Marta Filizola.

https://doi.org/10.1016/j.bpj.2022.08.018

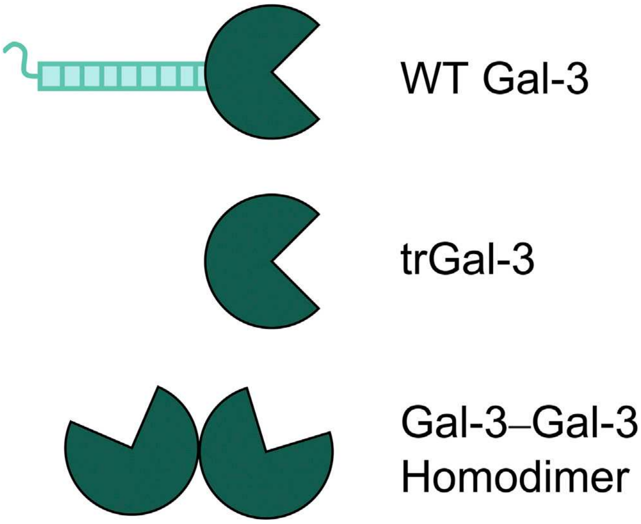

FIGURE 1 Schematic of proteins constructed from the Gal-3 CRD. WT Gal-3 contains one CRD bound to an N-terminal domain that promotes oligomeric assembly. Several engineered variants were tested, including a truncated Gal-3 CRD lacking the N-terminal domain (trGal-3) and a Gal-3 CRD homodimer (Gal-3–Gal-3).To see this figure in color, go online.

nine proline-glycine-rich non-triple helix collagen-like repeat units (13) and an N-terminal peptide with two serine residues as substrates for phosphorylation.(14) The N-terminal domain is highly flexible, which altogether confers unique oligomerization capabilities to Gal-3 (15,16). The N-terminal domain is known to bind neighboring Gal-3 CRDs, allowing the formation of pentamers and higher-order supramolecular lattice structures (14,17).

Ganglioside GM1 is a glycolipid binding partner of Gal-3 found on the outer leaflet of the plasma membrane. GM1 is composed of a sphingosine core and a branched pentasaccharide motif (Galβ1-3GalNAcβ1-4(Neu5Acα2-3)Galβ1-4GlcβCer) that extends above the surface of the cell membrane. GM1 is found in various cell types, but it is highly enriched in neuronal cell membranes in which gangliosides account for up to 10%–12% of the total lipid content (18,19). Cellular studies have shown that Gal-3 plays a role in membrane-mediated signaling through affinity to the cell surface, potentially through interactions with GM1 (20,21). Interactions between GM1 and Gal-3 mediate neuronal cell growth and adhesion as well as regulating metastasis in carcinomas (22–24); therefore, it is essential to understand how Gal-3 binds GM1 in a lipid membrane. Crystallographic studies have elucidated the atomistic structures of the Gal-3 (25,26) CRD bound to small glycan ligands; however there is limited information about these galectin structures as they interact with GM1 in a membrane context.

The study aimed to determine the structure of Gal-3 binding in situ to a lipid membrane monolayer model containing ganglioside GM1, which bridges several gaps in knowledge. First is the uncertainty regarding Gal-3's binding orientation relative to the membrane, particularly the N-terminal domain's role in membrane interactions. Another question is how the balance of protein affinity and membrane crowding determines galectin surface density, which is relevant for understanding the galectin lattices that form on the surface of cell membranes. Finally, given the importance of galectin-mediated macromolecule complexes for cell-signaling events, it is critical to understand how Gal-3 can associate with other proteins while simultaneously bound to GM1 at the membrane surface. To determine the structure of membrane-bound Gal-3, we used liquid surface X-ray reflectivity (XR) from a lipid monolayer assembled on an aqueous subphase. XR is a valuable technique for determining the electron density profile of a lipid membrane and the associated proteins bound at the membrane surface. We used this method to elucidate the orientation and surface density of Gal-3 bound to the membrane, and provide information about membrane structure.

Overall, in this work, we provide experimental evidence to support an atomistic model for the structure of Gal-3 bound in situ to a membrane containing GM1. Electron density profiles indicate that the Gal-3 CRD is closely adsorbed to the GM1 glycans, while most of the N-terminal domain extends away from the membrane. Gal-3 can bind the membrane at high density, with one molecule bound per approximately 2130 $Å^2$ of the membrane. In this in vitro system, Gal-3 covered ~50% of the membrane surface, reaching the limits predicted by random sequential adsorption models. These interactions between Gal-3 and GM1 observed in this study may help understand how Gal-3 can affect biologically relevant processes such as neuronal growth or adhesion (24,27).

MATERIALS AND METHODS

Materials

1,2-Dipalmitoyl-sn-glycero-3-phosphocholine (DPPC) and ganglioside GM1 were purchased from Avanti Polar Lipids (Alabaster, AL) as a dry powder. DPPC and GM1 stock solutions were prepared at 2–3 mg/mL in 8:2 v/v chloroform:methanol and sonicated for 30 seconds. A spreading solution of 0.2 mg/mL with the desired molar ratio (80:20, 85:15, 90:10, 95:5, or 100:0) of DPPC:GM1 in 8:2 chloroform to methanol was prepared for Langmuir trough experiments. Galectin proteins were expressed and purified according to previously published methods (23,28). Lyophilized proteins were dissolved in water at 1 mg/mL. Protein aliquots were frozen and used immediately once thawed.

Langmuir trough assays

Experiments were performed using a Nanoscience Instruments KSV-Nima extra-small Teflon trough (50 × 260 mm) with symmetric movable Delrin barriers and a Wilhelmy plate balance. The 46-mL subphase was pure 18 MΩ water at room temperature. A lipid spreading solution containing various mixtures of DPPC:GM1 with 0.5 mol % Texas Red-DHPE was deposited onto the air/water interface, 10 minutes were allowed for solvent evaporation, and the barriers were compressed until the surface pressure reached 20 mN/m. Protein was injected to reach a final concentration of

12.5 μg/mL in the subphase. After protein injection, the barrier expansion was fixed to create a constant-area system where protein insertion would increase surface pressure. Fluorescence microscopy images were taken using an Olympus IX73 inverted microscope with a 10× objective, ORCA Spark camera, and X-Cite mini+ LED light source. Images were collected and processed using Olympus cellSens Standard software. Images were collected before protein injection and 5 h after protein injection.

XR data collection

Liquid surface scattering experiments were performed at the Advanced Photon Source at Argonne National Labs (Sector 15 NSF's ChemMatCARS) using a 20-mL Langmuir trough (6.5 × 6.5 cm^2) filled with degassed water. Surface pressure was monitored with a Wilhelmy plate balance (KSV Instruments, Finland), and the experiments were performed at room temperature (23.5°C ± 0.5°C). Langmuir trough experiments were performed under constant-area conditions, where protein binding caused an increase in surface pressure. Lipids were deposited on the air/water interface to a surface pressure of 20 mN/m, and 10 min was allowed for solvent evaporation before proteins were injected into the subphase to a final concentration of 12.5 or 60 μg/mL.

During data collection, gaseous oxygen content was maintained at $< 2\%$ to prevent background X-ray scattering and oxidative beam damage to the monolayer. This was achieved by sealing the trough in a canister and purging the system with helium gas. X-ray wavelength was 1.24 Å, and the incoming X-ray beam footprint's dimensions on the liquid surface was ~1 × 3–10 mm^2 for XR. As a precaution against beam damage, the trough was systematically translated by 1 mm horizontally perpendicular to the X-ray beam after each scan. A Dectris PILATUS 100 detector was used to detect X-ray scattering, and X-ray scattering images were integrated using Python software (https://github.com/weibu/Liquid_Surface_ChemMatCARS).

Liquid surface XR theory and data analysis

XR was used to measure the electron density of materials deposited at the air/water interface on a Langmuir trough. X-ray scattering theory has been fully described previously (29–32), and only a brief summary is provided here. By measuring the intensity of reflected X-rays, one can deduce detailed information on the electron density distribution normal to the interface, $\rho(z)$, laterally averaged over both the ordered and disordered parts of the film. The reflectivity is defined as the ratio of reflected to incident beam intensities, in a specular geometry, as a function of the vertical momentum transfer vector $q_z = (4\pi/\lambda)\ \sin\theta$, where θ is the incident angle of the X-ray on the surface. Finally, the reflectivity curve can be analyzed to obtain the in-plane averaged electron density distribution normal to the interface.

The data were collected by tilting a germanium monochromator crystal to deflect the beam and change the angle of incidence on the sample. Intensities were collected over the range $0.01 < q_z < 0.8$ Å^{-1}, background subtracted, and normalized to incident beam flux. Data presented are divided by the Fresnel reflectivity (scattering from infinitely sharp air-water interface) (R_F) with error bars representing one standard deviation error for each data point. Division by the Fresnel reflectivity provided better visualization of the XR data.

The data were analyzed using a model-free approach based on cubic B-splines to obtain the electron density profile normal to the interface (33). The coefficients in the B-spline series were determined by constrained nonlinear least-squares methods, in which the smoothest solution with the lowest χ^2 goodness of fit was chosen. Over several thousand refinements were performed within the parameter space and a family of models is presented for each reflectivity dataset, all of which satisfy $\chi^2 \le \chi^2_{\text{min}} + 10\%$ with typical values of $\chi_{\text{min}}{}^2 < 10$.(34) The set of fits to each measurement fall within the shaded regions presented in the R/R_F versus q_z plots. The superposition of the profiles matching these fits yielded electron density "ribbons" (regions between the dotted lines on the XR graphs), which are a measure of the uncertainty in the real space structures.

A complementary model-dependent method was also used, where a "slab" model was used to obtain the electron density profile normal to the interface. The studied system was divided into layers, or slabs, of certain thickness, electron density, and the slabs were interconnected by interfacial roughness approximated by error functions. The parameters of this model were adjusted using program Motofit (35) to obtain lowest χ^2 values and reasonable values of the parameters. Parameter uncertainties were estimated using a finite difference approach with a covariance matrix describing the concavity of χ^2 with respect to each fit parameter. However, due to interdependence of the parameters, we expect that parameter errors may be underestimated in the reported data. The results are best interpreted with consideration given to both the model-independent and model-dependent fitting methods.

Molecular dynamics simulations

CHARMM-GUI (36) was used to build the pure-membrane systems containing 80:20 or 85:15 mol % DPPC:GM1. Each system was built with 50 Å of water on either side of the membrane and contained 0.15 M KCl. The 80:20 mol % DPPC:GM1 membrane was built using 168 DPPC and 42 GM1 lipid with 25,098 TIP3 waters into a rectangular box 80.94 × 80.94 × 140 Å in size. The 85:15 mol % DPPC:GM1 membrane was built with 204 DPPC, 36 GM1, and 29,267 TIP3 waters in an 86.6 × 86.6 × 170 Å rectangular box. For the 85:15 DPPC:GM1 system containing Gal-3 CRD, the protein coordinates were obtained from PDB (PDB: 3AYC), which contains the GM1 pentasaccharide bound to the Gal-3 CRD. The location of the crystallographically observed pentasaccharide was used to position the Gal-3 CRD onto an exposed GM1 glycan in the pure-membrane system that was assembled by CHARMM-GUI. The systems were parameterized with the CHARMM c36m forcefield (37), and simulations were performed using Gromacs 2021.2 (38). The system was simulated for 10 ns of production using 2-fs time steps, and the final 1 ns was used for analysis. The electron density of each membrane component was calculated using the Gromacs tool gmx density.

For all simulations, minimization was performed by steepest descent until the maximum force was less than 1000 kJ/(mol•nm). Equilibration was performed in six steps of 125, 125, 125, 250, 250, and 250 ps each, beginning with a force constant of 1000 kJ/(mol•nm^2) to restrain the lipids and gradually reducing the position restraints every step. For the systems containing protein, the protein was initially restrained with a force constant of 3000 kJ/(mol•nm^2) in the first equilibration step, with gradual reduction of the restraints in each of the following equilibration steps. The temperature was maintained at 303.15 K using the Berendsen thermostat and pressure was controlled using the Berendsen semi-isotropic barostat. Long-range electrostatics were calculated using particle-mesh Ewald (PME) and a Verlet cutoff scheme was applied with 1.2-nm distance for all nonbonding interactions. Bonds were constrained using LINCS. During production, the temperature and pressure were controlled with a Nose-Hoover and semi-isotropic Parrinello-Rahman thermostat and barostat, respectively.

Fitting XR results to determine trGal-3 binding orientation

trGal-3 XR results were used to model the orientation of the Gal-3 CRD bound onto the membrane. trGal-3 electron density was calculated using PDB (PDB: 5OAX). The protein was oriented relative to the membrane using the crystal structure of Gal-3 CRD bound to the GM1 pentasaccharide. The XR results were analyzed using a B-spline or box-model scattering length density (SLD) profile fit, assuming the lipid tails contained no solvent and the interfacial roughness was equal for the heads/tails and tail/air interfaces (3.0 Å).

To determine the electron density of the protein, all atoms were projected on to the *y-z* plane and a Voronoi tessellation algorithm was used to calculate the area of the protein on the membrane surface. For the Voronoi tessellation algorithm, the projected protein area was 966.6 Å^2, and a grid of points with 1 Å spacing was used to bound the protein. Any grid point within 2.8 Å of a projected atom position was removed to eliminate interior grid points. The value of 2.8 Å approximates the atomic diameters (van der Waals radius for hydrogen = 1.2 Å, carbon = 1.7 Å), which was optimized to match the volume calculated using the 0.73 cm^3/g approximation for globular soluble proteins (39). The Voronoi tessellation approach was applied on slices through the protein structure. Slices in the *y-z* plane were 1 Å thick in the *x* direction and any atoms with an *x* position within (R_{VDW} + slice thickness/2) = 1.9 Å were included in the slice.

Summing Voronoi tessellations of the *x* slices yielded the protein area as a function of *x*, which was integrated to determine the overall protein volume and calculate electron density. The XR-determined electron density distributions were compared before and after protein binding to determine the experimental electron density profile of the protein.

RESULTS AND DISCUSSION

WT Gal-3 binds to a model lipid membrane containing GM1

To study Gal-3 interactions with GM1, we used a model membrane system made from a lipid monolayer deposited at the air/water interface in a Langmuir trough. This in vitro model membrane has several strengths, including the ability to finely tune membrane composition and surface pressure (density of membrane-forming components), and measure protein interactions over an extended period of time (up to 12 h). We chose a simple lipid composition containing various ratios of GM1 and DPPC to probe the impact of GM1 concentration on Gal-3 binding specifically. X-rays can be scattered from the liquid surface to perform in situ XR. In these experiments, the membrane was first compressed to a target surface pressure, where surface pressure (π) was measured using a Wilhelmy plate suspended from a balance. We chose a starting surface pressure of 20 mN/m to form a membrane containing both ordered (liquid condensed) and disordered (liquid expanded) phase lipids, confirmed by fluorescence microscopy using a phase-sensitive dye (Fig. S1). The protein was injected into the aqueous subphase below the membrane and allowed to interact with the membrane for several hours.

One challenge of in vitro galectin experiments is the protein's tendency to embed into the lipid hydrocarbon tails non-specifically (40,41), which poses a challenge in capturing biologically relevant interactions between the CRD and the GM1 glycan. We tested a range of membrane compositions (0–20 mol % GM1) to combat this, with the rationale that the bulky glycan would deter the galectin proteins from embedding into the membrane by blocking access to the hydrophobic lipid tails. Langmuir trough experiments were performed to test WT Gal-3 binding to membranes composed of mixtures of DPPC and GM1 (Fig. 2). In experiments with the highest GM1 concentration (20 mol %), the increase in surface pressure ($\Delta\pi$ = 6.5 mN/m) indicates that WT Gal-3 bound the membrane.

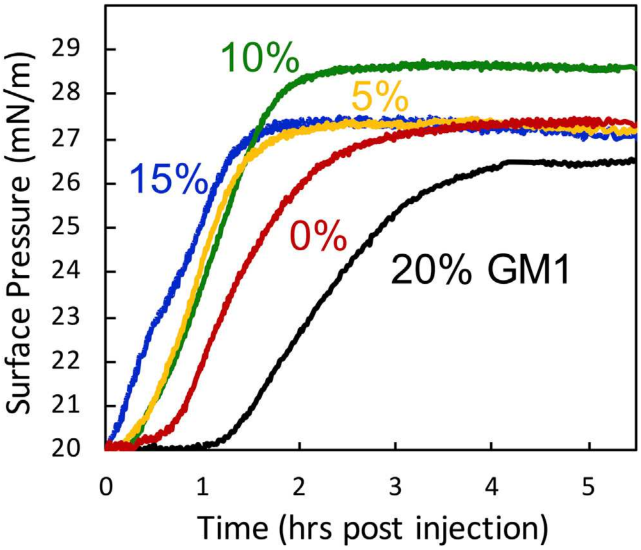

FIGURE 2 Surface pressure isotherms for 12.5 μg/mL WT Gal-3 insertion into a membrane composed of 0 (red), 5 (yellow), 10 (green), 15 (blue), or 20 (black) mol % GM1, with DPPC composing the remainder of the membrane. To see this figure in color, go online.

Interestingly, WT Gal-3 interacted with all membrane compositions, including those without GM1 (Fig. 2). Langmuir trough isotherm experiments cannot discern between protein embedding into the membrane via non-specific interactions with hydrophobic lipid tails or adsorbing to the membrane surface through specific interactions with the GM1 glycans. However, protein adsorption beneath the monolayer is expected to manifest as a smaller surface pressure increase than protein insertion into the lipid tails (42). At 20 mol % GM1, the surface pressure increase was less than that observed for interaction with a pure DPPC membrane ($\Delta\pi$ = 7.3 mN/m), suggesting that WT Gal-3 interactions were more likely to include specific contacts with the GM1 glycan when the GM1 concentration was high. As indicated by the changes in surface pressure, membrane binding was highest at 10 mol% GM1. However, this is likely due to a combination of specific interactions with GM1 and non-specific insertion into the lipid monolayer.

XR experiments were performed to resolve the position of Gal-3 bound to the lipid monolayer and confirm specific interactions with the GM1 glycans. XR can resolve layers of electron-dense material present at the air/water interface, including differences between protein and lipids. This is done by analyzing deviations of the measured reflectivity (R) from the Fresnel reflectivity of an ideal interface (R_F). The membrane can be described by electron density distribution (ρ) as a function of depth along the z axis, normal to the air/water interface. For ease of comparison between experimental and computational methods, the measured electron density was plotted after normalization to the solvent electron density ($\rho/\rho_{\mathrm{water}}$). $\rho/\rho_{\mathrm{water}}$ can be used to resolve the position of distinct chemical moieties in the monolayer due to the electron density difference between the solvent and hydrocarbon lipid tails ($\rho/\rho_{\mathrm{water}} = 0.97$), phospholipid heads ($\rho/\rho_{\mathrm{water}} = 1.32$), and glycans ($\rho/\rho_{\mathrm{water}} = 1.16$). For a homogenous protein layer completely excluding solvent, a $\rho/\rho_{\mathrm{water}}$ of 1.23 is expected (43). Protein adsorption beneath the monolayer rarely results in complete membrane coverage. The resulting $\rho/\rho_{\mathrm{water}}$ is expected to range between 1.0 and 1.23 depending on the density by which the protein covers the membrane and excludes solvent. The length of this $\rho/\rho_{\mathrm{water}}$ increase along the z axis will indicate the length of the protein layer adsorbed to the membrane. Furthermore, if the protein embeds into the lipids, it will change the average $\rho/\rho_{\mathrm{water}}$ in that region based on the molar ratio of protein to lipid components.

$\rho/\rho_{\mathrm{water}}$ was determined using model-independent fitting of normalized reflectivity (R/R_F) as a function of the scattering vector (q_z) (Fig. 3 *A*). Reflectivity data were collected from a pure 80:20 mol % DPPC:GM1 membrane, and 6 h after addition of 12.5 or 60.0 μg/mL WT Gal-3. There is agreement between the data and the fit for each dataset, indicating confidence in the resulting $\rho/\rho_{\mathrm{water}}$ models.

From the $\rho/\rho_{\mathrm{water}}$ distribution of a pure 80:20 DPPC:GM1 membrane (Fig. 3 *B* and *C*, black trace), the hydrocarbon tails can be observed from approximately −20 to −5 Å, phospholipid heads from −5 to +3 Å, and glycans from +3 to +16 Å. In these plots, $z = 0$ is defined as the center of the lipid heads. WT Gal-3 was observed adsorbing to the 80:20 DPPC:GM1 membrane, shown by the increased $\rho/\rho_{\mathrm{water}}$ at z distances of ∼16–65 Å (Fig. 3 *B* and *C*). As expected, the protein appears to bind the membrane through interfacial interactions with the GM1 glycans, not through

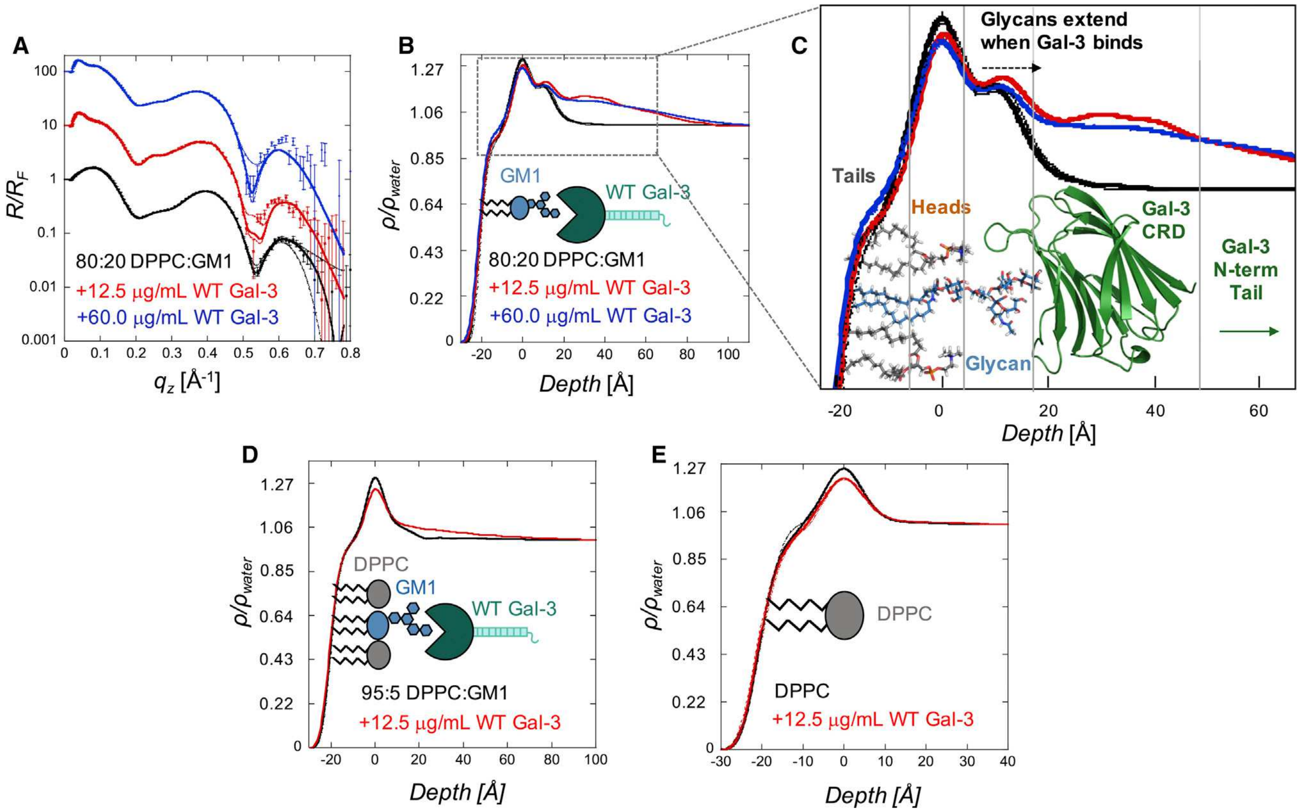

FIGURE 3 (*A–C*) X-ray reflectivity (XR) data collected from a lipid monolayer composed of pure 80:20 mol % DPPC:GM1 and with 12.5 or 60 μg/mL WT Gal-3. (*A*) Normalized reflectivities (R/R_F) are plotted as a function of the scattering vector (q_z). Measured reflectivities are represented as points with experimental error, and the model is shown as lines. The plot shows the best-fit model (solid line) and the outer bound of all models within 10% of the lowest χ^2 as dashed lines on either side of the best-fit line. The lowest χ^2 models each lie on top or near the best-fit model, indicating high confidence in the fit. Reflectivities are shown with a vertical offset for clarity. (*B*) Normalized electron density profiles ($\rho/\rho_{\mathrm{water}}$) that result from reflectivity fitting are plotted as a function of depth normal to the air/water interface, where zero is defined as the center of the lipid head group. The lowest χ^2 model is shown as a solid line; all models within 10% of the lowest χ^2 are plotted with a dashed line, although this is nearly overlaying the best-fit model. A cartoon of GM1 and WT Gal-3 is overlaid onto the electron density profile. (*C*) Inset from (*B*), showing the molecular structures of DPPC, GM1, and the Gal-3 CRD aligned with the electron density profile. The Gal-3 CRD was modeled from PDB: 3AYC. DPPC and GM1 structures were taken from a membrane built in CHARMM-GUI (36). (*D* and *E*) $\rho/\rho_{\mathrm{water}}$ profiles fitted from XR results of 12.5 μg/mL WT Gal-3 interacting with a membrane composed of 95:5 DPPC:GM1 (*D*) or pure DPPC (*E*). Cartoon images of DPPC, GM1, and WT Gal-3 are overlaid. Reflectivity fits for (*D*) and (*E*) are shown in Fig. S3.To see this figure in color, go online.

embedding into membrane lipids. The protein ρ/ρ_{water} indicates the amount of protein adsorbed to the membrane surface. Comparing the concentrations of 12.5 μg/mL with 60 μg/mL WT Gal-3 in the water subphase, there was no significant change to the ρ/ρ_{water} profile, suggesting both concentrations resulted in similar amount of protein adsorbed to the membrane and binding was saturated at 12.5 μg/mL.

Model-dependent fitting was used for each dataset to quantitate the length of the protein layer (Fig. S2 and Table S1). Model-dependent fitting is performed by building layers of electron density to represent each unique chemical composition in the membrane, one layer each for the hydrocarbon tails, phospholipid heads, glycans, and protein. Each layer is parameterized with a length, electron density, and interfacial roughness to account for interfaces between layers.

Results from the model-dependent fitting show the WT Gal-3 protein was best fit with two separate layers of distinct electron density, totaling ~50 Å in length altogether. The first layer, likely representing the Gal-3 CRD, extends 26.9 ± 0.4 Å away from the glycans, while the second layer, likely representing Gal-3 N-terminal domain, extends 22.5 ± 0.9 Å away from the CRD and into the water subphase. Crystal structures of isolated Gal-3 CRD (lacking the chimeric domain) show a maximum expected length of ~30 Å (PDB: 3AYC) (25), supporting our observation of distinct regions occupied by the Gal-3 CRD and the N-terminal domain.

As a result of Gal-3 binding, the glycans extend toward the water subphase. In the pure membrane, the glycan layer has a length of 12.8 ± 0.1 Å; however, upon protein binding, this increases to 13.5 ± 0.1 Å. This glycan extension is also clearly observed in the SLD results from model-independent fitting (Fig. 3 *C*). The implication is that, in the pure-membrane system, the glycans have a compact configuration and are "matted down" on the surface of the membrane to optimize hydrogen bonding with themselves and the phosphocholine headgroups. In contrast, when Gal-3 binds, the glycans extend away from the monolayer and form favorable contacts with the Gal-3 CRD.

Gal-3 interactions with a membrane containing 5% GM1 led to a sparsely populated protein layer extended beneath the glycans (Figs. 3 *D* and S4; Table S2). From the model-dependent fitting, there was 58% less electron density associated with the protein compared with Gal-3 bound to a membrane containing 20% GM1 (Table S1; Fig. S2). Gal-3 binding to a 10% GM1 membrane was similar to the 5% GM1 results (Fig. S4 Table S2). Finally, in experiments with a pure DPPC membrane, no protein was adsorbed to the membrane surface (Fig. 3 *E*), as indicated by small changes in the electron density profiles. However, a slight decrease in lipid headgroup ρ/ρ_{water} indicates Gal-3 was embedded into the membrane and formed non-specific contacts with the DPPC lipids. Overall, this suggests that Gal-3 forms specific interactions with the GM1 glycans, and membrane surface coverage is dependent on the amount of GM1 in the membrane.

Gal-3 N-terminal domain contacts CRD but not membrane

As mentioned in the introduction, Gal-3 is a chimera-type galectin with a C-terminal CRD and an N-terminal domain that promotes oligomerization (17). To discern the role of the N-terminal domain on membrane binding, we tested a series of engineered variants (Fig. 1) including a truncated Gal-3 containing only the CRD (trGal-3) and a covalently linked Gal-3 CRD homodimer (Gal-3–Gal-3).

Langmuir trough assay experiments with an 80:20 DPPC:GM1 membrane indicate strong interaction for all constructs, suggesting that the N-terminal domain is not essential for membrane binding (Fig. 4 *A*). However, the N-terminal domain seems to contribute to membrane interactions because trGal-3 required more time to reach its surface pressure plateau than WT Gal-3.This supports previous findings that removing the N-terminal domain reduces Gal-3 affinity to the cell surface, increasing the K_d from 0.74 to 3.1 μM (22). However, this delay in membrane binding was not observed for Gal-3–Gal-3. We interpret these binding kinetics to indicate additional Gal-3 CRDs drive rapid saturation on the membrane. However, the N-terminal domain likely contributes to a more dynamic and complex Gal-3 oligomerization equilibrium with a slower on-rate.

XR was used to determine the structure of each construct bound in situ to the membrane surface. trGal-3 formed a shorter protein layer (27.6 ± 0.3 Å) than the WT Gal-3, shown by model-independent and -dependent XR fitting results (Fig. 4 *B* and *C*). The Gal-3–Gal-3 homodimer accommodated both CRDs oriented in close contact with the membrane (Fig. 4 *B–D*), forming a protein layer only 31 ± 0.7 Å in length. Compared with the ~50 Å protein layer observed for WT Gal-3, this finding supports the interpretation that the CRD contacts GM1, while the N-terminal domain extends away from the membrane. Furthermore, this supports the interpretation that the second electron-dense layer of 23 Å can be attributed to the N-terminal domain, and is corroborated by models constructed from SAXS measurements of WT Gal-3 (44). We suggest this supports a model for a compacted N-terminal domain configuration and WT Gal-3 oligomerization on the membrane surface. If the N-terminal domain was behaving as a fully extended Flory chain in a good solvent, it would extend ~60 Å in length (45). The XR model only provides strong evidence for ~23 Å of well-defined electron density. However, given that XR data represent an average of many spatial/temporal states, we expect the model represents an ensemble containing a

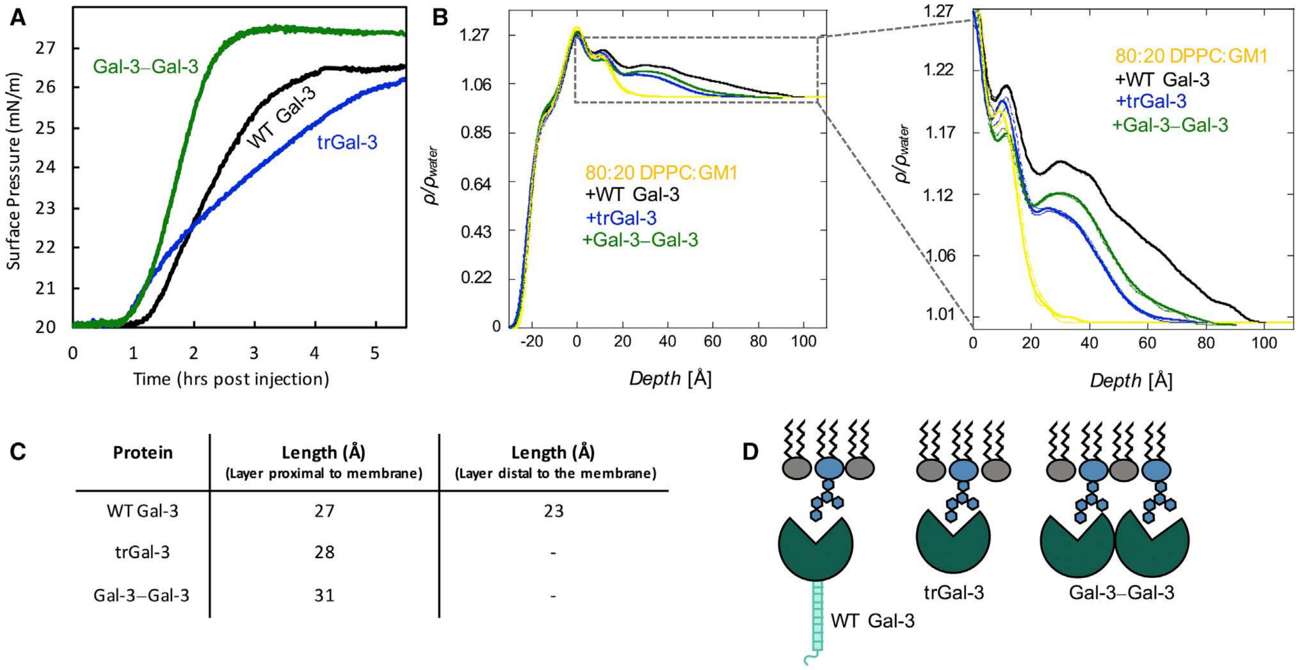

Protein	Length (Å) (Layer proximal to membrane)	Length (Å) (Layer distal to the membrane)
WT Gal-3	27	23
trGal-3	28	-
Gal-3–Gal-3	31	-

FIGURE 4 Engineered galectin variants accommodate protein-protein interactions while bound to GM1. Surface pressure isotherms (*A*) and ρ/ρ_{water} profiles fitted from model-independent XR fitting (*B*) of 12.5 μg/mL Gal-3–Gal-3 (green) and trGal-3 (blue) binding to an 80:20 DPPC:GM1 membrane. Pure membrane (yellow), and WT Gal-3 (black) are also overlaid. Reflectivity fits are shown in Fig. S3. (*C*) Fitted protein lengths obtained from model-dependent fitting (Fig. S2 and Table S1). WT Gal-3 data was best fit with two separate layers added in tandem, shown as two separate lengths in the table. Parameter errors are approximately ±1 Å. (*D*) Model of engineered galectin variants binding the membrane. To see this figure in color, go online.

range of extended to compact N-terminal domain configurations present at the membrane.

Interestingly, trGal-3 has 25% less protein electron density in the region attributed to the CRD compared with WT Gal-3 (Fig. 4 *B*; Table S1). We suggest two possible reasons for this. The first is that the N-terminal domain may increase Gal-3's affinity for the membrane without directly interacting with GM1 (22). Higher membrane affinity would increase WT Gal-3 binding, causing higher averaged electron density where the CRD is bound. The second reason is that small portions of the N-terminal domain may be stably associated with the CRD, increasing the electron density in that region. A crystal structure (PDB: 6FOF) shows 14 amino acids from the N-terminal domain form strong contacts with the Gal-3 CRD (44). NMR studies indicate that most of the N-terminal domain is disordered but that some residues have significantly reduced mobility in the region proximal to the CRD (46–48). Furthermore, interactions between the N-terminal domain and the CRD are observed to modulate Gal-3 oligomerization and glycan interactions (15).

To determine the electron density contributed by the N-terminal domain, we compared our XR results with a calculated electron density for a published Gal-3 CRD crystal structure (PDB: 3AYC) (25) (Fig. S5). Modeling results indicate that the N-terminal domain contributes electron density from 50–100 Å (reported in terms of the "Depth" scale in Fig. 4 *B*). This suggests the N-terminal domain interacts with the Gal-3 CRD distal to the membrane and does not interact with GM1 or the membrane surface.

Molecular modeling of Gal-3 CRD bound to the membrane

To correlate an atomistic model with the XR results, we performed a preliminary molecular dynamics simulation of the Gal-3 CRD bound to GM1 in a membrane. The starting structure of the simulation was based on the published crystal structure of the Gal-3 CRD bound to the GM1 pentasaccharide (PDB: 3AYC) (25). Guided by this structure, the Gal-3 CRD was positioned onto a GM1 molecule embedded into an 85:15 DPPC:GM1 membrane built with 204 DPPC, 36 GM1, and 29,267 TIP3 waters in an 86.6 × 86.6 × 170 Å rectangular box using CHARMM-GUI (36) (Fig. 5 *A* and *B*). The simulation was built with 15 mol % GM1 in the membrane because the protein was more easily accommodated among the crowded glycan environment on the membrane surface. However, a pure 80:20 DPPC:GM1 membrane (without protein) was also simulated and compared with experimental XR results.

The electron density of the simulated membrane showed consensus with the profiles derived from XR results (Fig. 5 *C* and *D*). However, the simulated membranes had slightly lower electron density for the phospholipid heads and more roughness between the head and glycan layers. These slight differences may be due to the XR experiments being

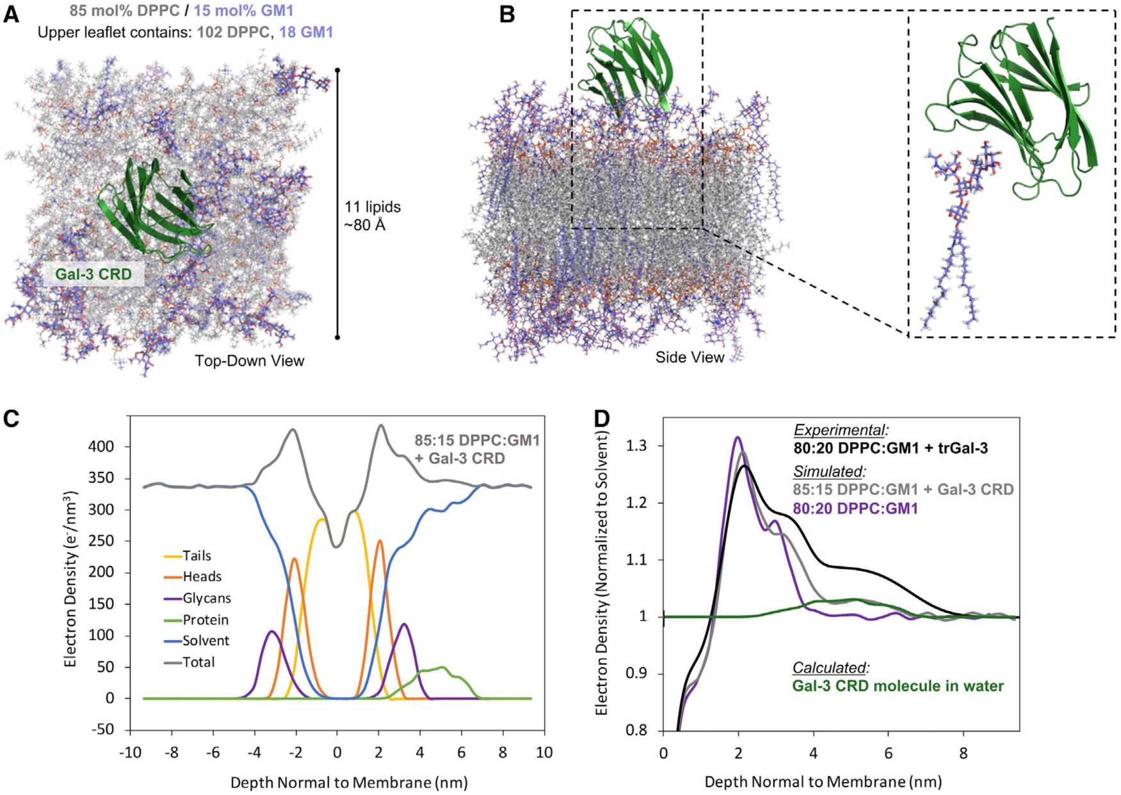

FIGURE 5 Top-down (*A*) and side (*B*) views of molecular dynamics system built using 85:15 mol % DPPC:GM1 membrane with one Gal-3 CRD molecule bound to a GM1. Inset shows orientation of the Gal-3 CRD bound to a single GM1 molecule. (*C*) Calculated electron density of each chemical moiety is plotted as a function of depth normal to the membrane, with zero as the center of the lipid bilayer. The sum of all components is shown in gray. (*D*) The electron density profile calculated from the simulated systems is plotted with the experimental electron density derived from XR of trGal-3 bound to a membrane containing 20 mol % GM1. For comparison, simulated electron density is also shown for a pure 80:20 mol % DPPC:GM1 membrane (purple) and a single Gal-3 CRD in water (green).To see this figure in color, go online.

performed with a lipid monolayer, while the simulations were performed with a lipid bilayer (49). The electron density was calculated for each chemical moiety (hydrocarbon tails, phospholipid heads, glycans, and protein), and the results generally align with the layers derived from model-dependent XR fitting.

Using the simulation, the electron density was calculated for a single Gal-3 CRD molecule in the predicted orientation for GM1 binding (Fig. 5 *D*). The electron density profile generally matches the protein layer observed from XR modeling of trGal-3 bound to 80:20 DPPC:GM1. The magnitude of the simulation profile is lower because the system was constructed with lower density of bound protein compared with the experimental system. The shape of the XR profile is a highly accurate representation of protein electron density averaged from billions of molecules in the path of the X-ray beam. In contrast, this simulation-derived profile is based on the position of a single molecule averaged over a short simulation time.

We also performed a Voronoi tessellation algorithm on slices through the three-dimensional protein structure to calculate electron density of the membrane-bound Gal-3 CRD (Fig. S5). The calculated Gal-3 CRD volume was 18,756.5 Å^3, which is within 1% of the predicted volume based on amino acid sequence and the standard density of globular proteins (0.73 cm^3/g) (39). This corresponds to an electron density of 0.44 $e^-/\text{Å}^3$. Overall, the calculated protein electron density was a good match to the experimental results, supporting an atomistic model describing the Gal-3 CRD binding the GM1 in a membrane.

In addition to Gal-3 interactions with GM1 glycans, we also observed a few close contacts between the Gal-3 CRD and DPPC headgroups, which may help to stabilize protein interactions with the membrane (Fig. S6). However, this will need further investigation with more extended molecular dynamics simulations to determine if the contacts persist over time. The binding orientation of the Gal-3 CRD predicted from crystallography indicates that the loops containing asparagines 141, 166, and 167 would be in proximity to form energetically favorable polar contacts with the lipid headgroups.

Estimated surface coverage of Gal-3 on the membrane

The surface density of membrane-bound Gal-3 likely influences cell signaling through Gal-3 oligomerization and supramolecular organization. Previous isothermal titration calorimetry and surface plasmon resonance experiments showed that Gal-3 binds free GM1 with a K_d of ~57–62 μM (25). However, we were curious to understand the interplay between GM1 membrane content and Gal-3 surface coverage, especially considering the limited space on the surface of the membrane. Increasing the protein concentration ~5× (from 12.5 to 60 μg/mL) did not increase Gal-3 surface density (Fig. 3), suggesting that protein concentration was not a limiting factor in these experiments.

From the XR results (Figs. 3, S2, and S4; Tables S1 and S2), it is evident that WT Gal-3 membrane coverage is dependent on GM1 concentration. A similar trend was observed for trGal-3 binding membranes with various GM1 compositions (Fig. S4; Table S2). In our Langmuir trough experiments with 12.5 μg/mL WT Gal-3 and a membrane containing 20% GM1, there is ~9.5 nmol of Gal-3 CRD and ~3.5 nmol of GM1 available for interactions. Therefore, the amount of GM1 is likely a limiting factor for Gal-3 binding.

Using protein electron density values determined from XR measurements, we can estimate Gal-3 surface coverage on a membrane containing 20% GM1. We used the electron density profile of the simulated 80:20 DPPC:GM1 membrane and added incrementally increasing quantities of calculated Gal-3 CRD electron density (Fig. 6). Comparing the simulated data with the experimental, we predict that about three protein molecules are bound for the area of membrane in the simulation (6400 Å^2, ~11 × 11 lipids in size), which equates to one protein bound per ~2130 Å^2. Surface coverage estimations were also performed based on fitting the XR data using calculated protein density and area from Voronoi tessellation calculations (Table S3). Our estimates range from 45%–56% coverage, which generally agrees with a simple division of the observed WT Gal-3 protein electron density by the theoretical maximum protein electron density that could be observed with 100% membrane coverage (0.12/0.23 = 52% coverage).

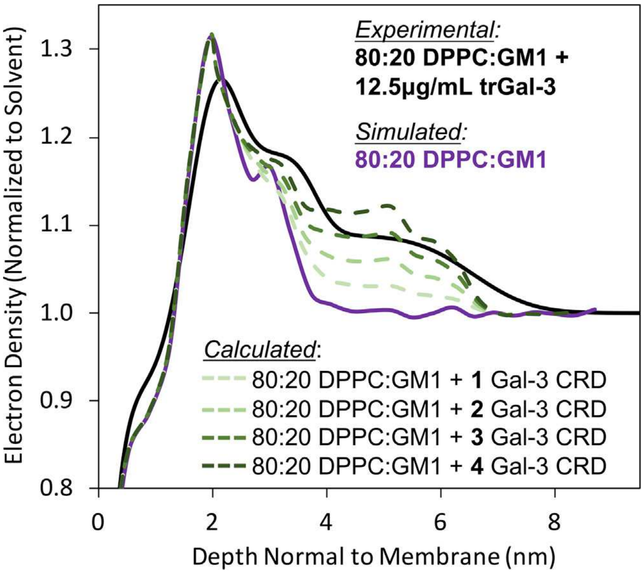

FIGURE 6 Estimation of Gal-3 surface coverage on a membrane containing 20 mol % GM1. The calculated Gal-3 CRD electron density was added to simulated 80:20 mol % DPPC:GM1 membrane. Additional copies of the protein electron density were added and compared with the experimental electron density for 80:20 mol % DPPC:GM1 membrane with 12.5 μg/mL trGal-3.To see this figure in color, go online.

Comparing this result with the literature, we find that Gal-3 membrane coverage matches the theoretical maximum of 54.67% predicted for random sequential adsorption of disks onto a two-dimensional surface (50). This adsorption limit is due to steric overlaps between neighboring adsorbed particles that are randomly distributed on the surface. We estimate that the disk shape is a reasonable approximation for the Gal-3 CRD. Disk dimers, such as the Gal-3–Gal-3 homodimer, also exhibit a maximum theoretical adsorption of 54.7% (51).

The theory of random sequential adsorption has two key assumptions that are relevant to consider in our system. The first assumption is that the particles can adsorb anywhere on the surface; in other words, the surface is homogeneous (52). Gal-3 did not reach the maximum theoretical adsorption when binding a membrane containing 5 or 10 mol % GM1, suggesting these concentrations are insufficient for the membrane to appear homogeneous to interacting Gal-3 molecules. The second assumption is that particles cannot rearrange once adsorbed onto the surface, meaning they hold a fixed location on the membrane once bound (52). However, in a theoretical system where disk-shaped particles can rearrange after adsorption, the maximum surface coverage may approach up to 85%, although the surface will likely have crystalline characteristics at this coverage density (53). At the low membrane surface pressures of 20–30 mN/m used in these experiments, the lipids exist in a mixture of liquid condensed and liquid expanded states (Fig. S1). This suggests that the GM1 molecules should have free two-dimensional diffusion around the membrane via the liquid expanded state. Interestingly, for all GM1 concentrations tested, Gal-3 adsorption never went above the estimated 54.7% for random sequential adsorption, suggesting that Gal-3 is not moving laterally around the membrane once bound. Furthermore, this indicates that Gal-3 does not assemble into a densely packed in-plane ordered conformation while forming supramolecular assemblies on the membrane surface. Higher GM1 concentrations could possibly induce a crystalline assembly, but higher GM1 concentrations are highly unlikely to occur in a biological system. Overall, the observed Gal-3 packing density is generally consistent with prevailing models for Gal-3 oligomerization and amorphous lattice formation (54), but does not uniquely support a specific assembly model.

CONCLUSIONS

We report the first direct observation of Gal-3 bound to GM1 in a membrane. This work provides mesoscale structural information about Gal-3/membrane interactions, aiming to bridge the gap between the atomistic X-ray crystallography structures and the micro-scale cell microscopy studies. Using liquid surface XR from a lipid monolayer, we observed Gal-3 forming specific interactions with the glycans beneath the surface of membranes containing 5–20 mol % GM1. The protein formed a layer that extended ~50 Å beneath the membrane, with 27 Å attributed to the CRD and the remaining 23 Å from the N-terminal domain.

The chimeric N-terminal domain is a distinguishing feature of Gal-3 that promotes protein oligomerization. We find that the Gal-3 CRD alone is sufficient for binding the membrane; however, binding is stronger when the N-terminal domain is present. Using Voronoi tessellation to model the XR results, we confirm previous work (44) showing that a portion of the N-terminal domain directly contacts the CRD, while the remainder extends away from the membrane and is available to participate in protein-protein interactions. Therefore, the N-terminal domain does not form direct interactions with the lipids, including the GM1's pentasaccharide chain.

We used molecular dynamics simulations and a Voronoi tessellation algorithm to model the electron density of membrane-bound Gal-3 compared with the XR results. Overall, our model agrees with the measured electron density profile from the XR results, suggesting a plausible orientation for Gal-3 binding to a membrane containing GM1. By comparing the modeled system with the experimentally derived electron density profile, we estimate one Gal-3 protein bound to every 2130 $Å^2$ of the membrane surface. This equates to ~50% surface coverage for membranes containing 20 mol % GM1, matching the predicted coverage limit based on random sequential adsorption theory.

In conclusion, Gal-3 forms specific interactions with GM1 glycans in a membrane context. Gal-3 has a highly flexible binding interface that can accommodate orthogonal protein-protein interactions, including oligomerization via the N-terminal domain. These interactions are thought to play important roles in neuronal cell-signaling applications, and we can see the structure-function relationship that facilitates this dynamic behavior. Gal-3 membrane surface coverage is limited by random sequential adsorption (maximum coverage of ~50%), indicating that a large amount of protein can bind the membrane, provided there is sufficient GM1. Overall, this structural information is essential for understanding of Gal-3/GM1 interactions and their roles in cell communication.

SUPPORTING MATERIAL

Supporting material can be found online at https://doi.org/10.1016/j.bpj.2022.08.018.

AUTHOR CONTRIBUTIONS

H.-J.G., C.V.Z., and J.M. designed research and the original concept for the paper. C.V.Z., Y.W., and D.B. collected Langmuir trough and microscopy data. C.V.Z., J.M., Y.W., and D.B. collected XR data and performed the analysis. C.V.Z. performed the molecular dynamics simulations. E.W. performed Voronoi tessellation analysis. C.V.Z. wrote the manuscript and made the figures. C.V.Z., J.M., Y.W., D.B., and E.W. edited and revised the manuscript.

ACKNOWLEDGMENTS

The authors would like to express sincere appreciation for the careful evaluation and feedback given by Prof. Herbert Kaltner, Dr. Joachim Manning, and Dr. Anna-Kristin Ludwig on this work. NSF provided support for J.M. to contribute to this project through their Independent Research and Development program. Any opinion, findings, conclusions, or recommendations expressed in this material are those of the authors and do not necessarily reflect the views of the National Science Foundation. D.B. was funded by the UCCS Undergraduate Research Academy and a UCCS College of Letters, Arts, and Sciences Research Assistant Scholarship. Y.W. was funded by the BRAiN Undergraduate Research Program (NIH award R25NS080685). XR data were collected at NSF's ChemMatCARS, which is supported by the Divisions of Chemistry (CHE) and Materials Research (DMR), National Science Foundation, under grant number NSF/CHE-1834750. The authors are grateful to beamline scientist Dr. Wei Bu for support during XR data collection.

DECLARATION OF INTERESTS

The authors declare no conflict of interest.

REFERENCES

1. Barondes, S., V. Castronovo, …, T. Feizi. 1994. Galectins: a family of animal β-galactoside-binding lectins. *Cell.* 75:597–598.
2. Liao, D.-I., G. Kapadia, …, O. Herzberg. 1994. Structure of S-lectin, a developmentally regulated vertebrate β-galactoside-binding protein. *Proc. Nat. Acad. Sci. USA.* 91:1428–1432.
3. Houzelstein, D., I. R. Gonçalves, …, F. Poirier. 2004. Phylogenetic analysis of the vertebrate galectin family. *Mol. Biol. Evol.* 21:1177–1187. https://doi.org/10.1093/molbev/msh082.
4. Hirabayashi, J., T. Hashidate, …, K. I. Kasai. 2002. Oligosaccharide specificity of galectins: a search by frontal affinity chromatography. *Biochim. Biophys. Acta Gen. Subj.* 1572:232–254. https://doi.org/10.1016/S0304-4165(02)00311-2.
5. Modenutti, C. P., J. I. B. Capurro, …, M. A. Martí. 2019. The structural biology of galectin-ligand recognition: current advances in modeling tools, protein engineering, and inhibitor design. *Front. Chem.* 7. https://doi.org/10.3389/fchem.2019.00823.
6. Modenutti, C., D. Gauto, …, M. A. Marti. 2015. Using crystallographic water properties for the analysis and prediction of lectin-carbohydrate complex structures. *Glycobiology.* 25:181–196. https://doi.org/10.1093/glycob/cwu102.
7. García Caballero, G., H. Kaltner, …, H.-J. Gabius. 2020. How galectins have become multifunctional proteins. *Histol. Histopathol.* 35:509–539.
8. Ludwig, A. K., H. Kaltner, …, H.-J. Gabius. 2019. Lectinology 4.0: altering modular (ga)lectin display for functional analysis and biomedical applications. *Biochim. Biophys. Acta Gen. Subj.* 1863:935–940. https://doi.org/10.1016/j.bbagen.2019.03.005.
9. Di Lella, S., M. A. Martí, …, D. A. Estrin. 2010. Linking the structure and thermal stability of β-galactoside-binding protein galectin-1 to

ligand binding and dimerization equilibria. *Biochemistry.* 49:7652–7658. https://doi.org/10.1021/bi100356g.

10. Nesmelova, I. V., E. Ermakova, …, K. H. Mayo. 2010. Lactose binding to galectin-1 modulates structural dynamics, increases conformational entropy, and occurs with apparent negative cooperativity. *J. Mol. Biol.* 397:1209–1230. https://doi.org/10.1016/j.jmb.2010.02.033.
11. Romero, J. M., M. Trujillo, …, S. Di Lella. 2016. Impact of human galectin-1 binding to saccharide ligands on dimer dissociation kinetics and structure. *Glycobiology.* 26:1317–1327. https://doi.org/10.1093/glycob/cww052.
12. Rabinovich, G. A., M. A. Toscano, …, G. R. Vasta. 2007. Functions of cell surface galectin-glycoprotein lattices. *Curr. Opin. Struct. Biol.* 17:513–520.
13. Cooper, D. N. W. 2002. Galectinomics: finding themes in complexity. *Biochim. Biophys. Acta Gen. Subj.* 1572:209–231. https://doi.org/10.1016/S0304-4165(02)00310-0.
14. Berbís, M. Á., S. André, F. J. Cañada, R. Pipkorn, H. Ippel, K. H. Mayo, D. Kübler, H.-J. Gabius, and J. Jiménez-Barbero. 2014. Peptides derived from human galectin-3 N-terminal tail interact with its carbohydrate recognition domain in a phosphorylation-dependent manner. *Biochem. Biophys. Res. Commun.* 443:126–131. https://doi.org/10.1016/j.bbrc.2013.11.063.
15. Zhao, Z., X. Xu, …, Y. Zhou. 2021. Galectin-3 N-terminal tail prolines modulate cell activity and glycan-mediated oligomerization/phase separation. *Proc. Natl. Acad. Sci. USA.* 118:1–11. https://doi.org/10.1073/pnas.2021074118.
16. Lin, Y.-H., D.-C. Qiu, …, J. Huang. 2017. The intrinsically disordered N-terminal domain of galectin-3 dynamically mediates multisite self-association of the protein through fuzzy interactions. *J. Biol. Chem.* 292:17845–17856. https://doi.org/10.1074/jbc.M117.802793.
17. Ahmad, N., H.-J. Gabius, …, C. F. Brewer. 2004. Galectin-3 precipitates as a pentamer with synthetic multivalent carbohydrates and forms heterogeneous cross-linked complexes. *J. Biol. Chem.* 279:10841–10847. https://doi.org/10.1074/jbc.M312834200.
18. Posse de Chaves, E., and S. Sipione. 2010. Sphingolipids and gangliosides of the nervous system in membrane function and dysfunction. *FEBS Lett.* 584:1748–1759. https://doi.org/10.1016/j.febslet.2009.12.010.
19. Tettamanti, G. 2003. Ganglioside/glycosphingolipid turnover: new concepts. *Glycoconj. J.* 20:301–317. https://doi.org/10.1023/B:GLYC.0000033627.02765.cc.
20. Kopitz, J., C. Von Reitzenstein, …, H.-J. Gabius. 1998. Galectin-1 is a major receptor for ganglioside GM1, a product of the growth-controlling activity of a cell surface ganglioside sialidase, on human neuroblastoma cells in culture. *J. Biol. Chem.* 273:11205–11211. https://doi.org/10.1074/jbc.273.18.11205.
21. Wang, J., Z.-H. Lu, …, G. Wu. 2009. Cross-linking of GM1 ganglioside by galectin-1 mediates regulatory T cell activity involving TRPC5 channel activation: possible role in suppressing experimental autoimmune encephalomyelitis. *J. Immunol.* 182:4036–4045. https://doi.org/10.4049/jimmunol.0802981.
22. Kopitz, J., S. Vértesy, …, H.-J. Gabius. 2014. Human chimera-type galectin-3: defining the critical tail length for high-affinity glycoprotein/cell surface binding and functional competition with galectin-1 in neuroblastoma cell growth regulation. *Biochimie.* 104:90–99. https://doi.org/10.1016/j.biochi.2014.05.010.
23. Ludwig, A. K., M. Michalak, …, V. Percec. 2019. Design–functionality relationships for adhesion/growth-regulatory galectins. *Proc. Natl. Acad. Sci. USA.* 116:2837–2842. https://doi.org/10.1073/pnas.1813515116.
24. Boscher, C., Y. Z. Zheng, …, I. R. Nabi. 2012. Galectin-3 protein regulates mobility of N-cadherin and GM1 ganglioside at cell-cell junctions of mammary carcinoma cells. *J. Biol. Chem.* 287:32940–32952. https://doi.org/10.1074/jbc.M112.353334.
25. Bian, C. F., Y. Zhang, …, D. C. Wang. 2011. Structural basis for distinct binding properties of the human galectins to Thomsen-Friedenreich antigen. *PLoS One.* 6. https://doi.org/10.1371/journal.pone.0025007.
26. Collins, P. M., K. Bum-Erdene, …, H. Blanchard. 2014. Galectin-3 interactions with glycosphingolipids. *J. Mol. Biol.* 426:1439–1451. https://doi.org/10.1016/j.jmb.2013.12.004.
27. Kopitz, J., M. Bergmann, and H.-J. Gabius. 2010. How adhesion/growth-regulatory galectins-1 and -3 attain cell specificity: case study defining their target on neuroblastoma cells (SK-N-MC) and marked affinity regulation by affecting microdomain organization of the membrane. *IUBMB Life.* 62:624–628. https://doi.org/10.1002/iub.358.
28. Vértesy, S., M. Michalak, …, H.-J. Gabius. 2015. Structural significance of galectin design: impairment of homodimer stability by linker insertion and partial reversion by ligand presence. *Protein Eng. Des. Sel.* 28:199–210. https://doi.org/10.1093/protein/gzv014.
29. Als-Nielsen, J., and K. Kjaier. 1989. X-ray reflectivity and diffraction studies of liquid surfaces and surfactant monolayers. *In* Phase Transitions in Soft Condensed Matter. Tormod Riste and David Sherrington, eds Plenum Press, New York and London, pp. 113–138.
30. Als-Nielsen, J., D. Jacquemain, …, L. Leiserowitz. 1994. Principles and applications of grazing incidence X-ray and neutron scattering from ordered molecular monolayers at the air-water interface. *Phys. Rep.* 246:251–313.
31. Jensen, T. R., and K. Kjaer. 2001. Structural properties and interactions of thin films at the air-liquid interface explored by synchrotron X-ray scattering. *In* Novel Methods to Study Interfacial Layers, pp. 205–254.
32. Kjaer, K. 1994. Some simple ideas on X-ray reflection and grazing-incidence diffraction from thin surfactant films. *Phys. B Condens. Matter.* 198:100–109.
33. Pedersen, J. S., and I. W. Hamley. 1994. Analysis of neutron and X-ray reflectivity data by constrained least-squares methods. *Phys. B Condens. Matter.* 198:16–23. https://doi.org/10.1016/0921-4526(94)90117-1.
34. Watkins, E. B., C. E. Miller, …, J. Majewski. 2009. Structure and orientational texture of self-organizing lipid bilayers. *Phys. Rev. Lett.* 102:1–4. https://doi.org/10.1103/PhysRevLett.102.238101.
35. Nelson, A. 2006. Co-refinement of multiple-contrast neutron/X-ray reflectivity data using MOTOFIT. *J. Appl. Crystallogr.* 39:273–276. https://doi.org/10.1107/S0021889806005073.
36. Lee, J., X. Cheng, …, W. Im. 2016. CHARMM-GUI input generator for NAMD, GROMACS, AMBER, OpenMM, and CHARMM/OpenMM simulations using the CHARMM36 additive force field. *J. Chem. Theor. Comput.* 12:405–413. https://doi.org/10.1021/acs.jctc.5b00935.
37. Owen, M. C., A. Karner, …, R. Vácha. 2019. Force field comparison of GM1 in a DOPC bilayer validated with AFM and FRET experiments. *J. Phys. Chem. B.* 123:7504–7517. https://doi.org/10.1021/acs.jpcb.9b05095.
38. Páll, S., M. J. Abraham, …, E. Lindahl. 2014. Tackling Exascale Software Challenges in Molecular Dynamics Simulations with GROMACS. Springer International Publishing.
39. Harpaz, Y., M. Gerstein, and C. Chothia. 1994. Volume changes on protein folding. *Structure.* 2:641–649. https://doi.org/10.1016/S0969-2126(00)00065-4.
40. Majewski, J., S. André, H.-J. Gabius…, 2015. X-ray reflectivity and grazing incidence diffraction studies of interaction between human adhesion/growth-regulatory galectin-1 and DPPE - GM1 lipid monolayer at an air/water interface. *Biochemistry (Mosc).* 80:943–956. https://doi.org/10.1134/S0006297915070135.
41. Lukyanov, P., V. Furtak, and J. Ochieng. 2005. Galectin-3 interacts with membrane lipids and penetrates the lipid bilayer. *Biochem. Biophys. Res. Commun.* 338:1031–1036. https://doi.org/10.1016/j.bbrc.2005.10.033.
42. Boucher, J., E. Trudel, …, C. Salesse. 2007. Organization, structure and activity of proteins in monolayers. *Colloids Surf., B.* 58:73–90. https://doi.org/10.1016/j.colsurfb.2007.03.019.
43. Mahieu, E., Z. Ibrahim, …, F. Gabel. 2020. The power of SANS, combined with deuteration and contrast variation, for structural studies of

functional and dynamic biomacromolecular systems in solution. *EPJ Web Conf.* 236:03002. https://doi.org/10.1051/epjconf/202023603002.

44. Flores-Ibarra, A., S. Vértesy, …, A. Romero. 2018. Crystallization of a human galectin-3 variant with two ordered segments in the shortened N-terminal tail. *Sci. Rep.* 8:1–11. https://doi.org/10.1038/s41598-018-28235-x.
45. Flory, P. J. 1969. Statistical Mechanics of Chain Molecules. Wiley, New York.
46. Birdsall, B., J. Feeney, …, R. C. Hughes. 2001. NMR solution studies of hamster galectin-3 and electron microscopic visualization of surface-adsorbed complexes: evidence for interactions between the N- and C-terminal domains. *Biochemistry.* 40:4859–4866. https://doi.org/10.1021/bi002907f.
47. Halimi, H., A. Rigato, …, F. Guerlesquin. 2014. Glycan dependence of galectin-3 self-association properties. *PLoS One.* 9:e111836. https://doi.org/10.1371/journal.pone.0111836.
48. Ippel, H., M. C. Miller, …, K. H. Mayo. 2016. Intra- and intermolecular interactions of human galectin-3: assessment by full-assignment-based NMR. *Glycobiology.* 26:888–903. https://doi.org/10.1093/glycob/cww021.
49. Mansour, H., D. S. Wang, …, G. Zografi. 2001. Comparison of bilayer and monolayer properties of phospholipid systems containing dipalmitoylphosphatidylglycerol and dipalmitoylphosphatidylinositol. *Langmuir.* 17:6622–6632. https://doi.org/10.1021/la0108454.
50. Feder, J. 1980. Random sequential adsorption. *J. Theor. Biol.* 87:237–254. https://doi.org/10.1016/0022-5193(80)90358-6.
51. Ciesla, M., and J. Barbasz. 2012. An RSA study of dimers. *J. Stat. Mech. Theor. Exp.* 2012:P03015. https://doi.org/10.1088/1742-5468/2012/03/P03015.
52. Evans, J. W. 1993. Random and cooperative sequential adsorption. *Rev. Mod. Phys.* 65:1281–1329. https://doi.org/10.1103/RevModPhys.65.1281.
53. Gray, J. J., D. H. Klein, …, B. A. Korgel. 2000. Nonequilibrium phase behavior during the random sequential adsorption of tethered hard disks. *Phys. Rev. Lett.* 85:4430–4433. https://doi.org/10.1103/PhysRevLett.85.4430.
54. Chiu, Y. P., Y. C. Sun, …, J. r. Huang. 2020. Liquid-liquid phase separation and extracellular multivalent interactions in the tale of galectin-3. *Nat. Commun.* 11. https://doi.org/10.1038/s41467-020-15007-3.